Applied Catalysis B: Environmental 208 (2017) 1–13

Contents lists available at ScienceDirect

Applied Catalysis B: Environmental

journal homepage: www.elsevier.com/locate/apcatb

Silver phosphate-based Z-Scheme photocatalytic system with superior sunlight photocatalytic activities and anti-photocorrosion performance

Tao Cai[a,b], Yutang Liu[a,b,*], Longlu Wang[c], Shuqu Zhang[c], Yunxiong Zeng[c], Jili Yuan[c], Jianhong Ma[a,b], Wanyue Dong[a,b], Chengbin Liu[c,**], Shenglian Luo[c]

[a] College of Environmental Science and Engineering, Hunan University, Lushan South Road, Yuelu District, Changsha 410082, PR China
[b] Key Laboratory of Environmental Biology and Pollution Control (Hunan University), Ministry of Education, Lushan South Road, Yuelu District, Changsha 410082, PR China
[c] State Key Laboratory of Chemo/Biosensing and Chemometrics, Hunan University, Lushan South Road, Yuelu District, Changsha 410082, PR China

ARTICLE INFO

Article history:
Received 13 December 2016
Received in revised form 17 February 2017
Accepted 19 February 2017

Keywords:
Ag_3PO_4
Z-Scheme photocatalytic system
Anti-photocorrosion
Photocatalytic degradation
Organic pollutant

ABSTRACT

The serious photocorrosion of silver phosphate (Ag_3PO_4) has limited its practical applications. In this work, we propose a strategy to suppress its photocorrosion by the construction of a Z-Scheme photocatalytic system, which composed of reduced graphene oxide-enwrapped Ag_3PO_4 (Ag_3PO_4@RGO) and La,Cr-codoped $SrTiO_3$ (La,Cr:$SrTiO_3$). Dramatically, this system shows superior anti-photocorrosion and photocatalytic performances in degradation of both RhB and 2,4-DNP. Especially for RhB, it can be completely degraded after only 5 min under intense sunlight irradiation. The improved photoactivity and anti-photocorrosion of Ag_3PO_4@RGO@La,Cr:$SrTiO_3$ can be attributed to the following: (i) The sufficient interfacial contact between Ag_3PO_4 and RGO is favorable to transfer the carriers and lengthen the lifetime of it; (ii) the package of Ag_3PO_4 with RGO could work as a sheltering layer to protect Ag_3PO_4 from photocorrosion. (iii) The aggregation of photogenerated holes in the VB of Ag_3PO_4 makes it a rich-hole region due to Z-Scheme electrons transport mechanism, which can protect Ag_3PO_4 from the photo-reduction. This strategy provides a new thought of protecting photosensitive semiconductor from photocorrosion and could regard as an efficient application method for environmental cleaning under natural sunlight irradiation. Furthermore, it even could be extended to outdoor or indoor air cleaning in the future.

1. Introduction

Solar energy-driven semiconductor photocatalysis has been considered to be one of the most potential ways to alleviate current energy and environment issues [1]. However, it is still a huge challenge for photocatalytic advanced oxidation technology in practical applications due to relatively low sunlight conversion efficiency. Silver orthophosphate (Ag_3PO_4) with high quantum efficiency of 90% at 420 nm has sparked widespread interests recently [2–4]. It would be one of the most promising photocatalysts for environment cleaning in practical applications [5]. Up to now, although Ag_3PO_4 is an efficient photocatalyst, it is still difficult to apply it in practice due to severe photocorrosion [6]. Therefore, the core problem is how to inhibit its photocorrosion before putting it into practical application.

When exposed to light, the Ag^+ can be easily reduced into metal Ag by excited electrons [5–7]. This could decrease the photocatalytic activity because of the loss of Ag_3PO_4 substance. In previous studies, to strengthen the anti-photocorrosion performance of Ag_3PO_4, various methods including carbon-based composite [8–10], semiconductor complex [11] and rejuvenation [12] have been proposed by researchers. It is worth mentioning that Teng et al. reported that the influence of light density to the stability of Ag_3PO_4[5,6]. They demonstrated that Ag_3PO_4 could become more stable when using natural weak light than artificial light. However, this approach could not solve the problem essentially and the improvement effect by virtue of above strategies is relatively small and very limited. The key to improve anti-photocorrosion performance of Ag_3PO_4 is to consume the electrons or transfer them away timely, thereby avoiding reaction of Ag^+ and electrons.

* Corresponding author at: College of Environmental Science and Engineering, Hunan University, Lushan South Road, Yuelu District, Changsha 410082, PR China.
** Corresponding author.
E-mail addresses: yt_liu@hnu.edu.cn (Y. Liu), chem_cbliu@hnu.edu.cn (C. Liu).

http://dx.doi.org/10.1016/j.apcatb.2017.02.065
0926-3373/

It is well known that photon-generated electrons in one component of Z-Scheme photocatalytic systems could directly recombine with photon-generated holes in another component [13–15]. This character could be used precisely for Ag_3PO_4 to improve its anti-photocorrosion performance by reasonable manipulation of electronic transmission. In addition, photogenerated carrier would aggregate on the surface of different components and make one semiconductor to be a rich-electron region and another become rich-hole region during photocatalytic reaction. In fact, the rich-hole micro-environment play a key role in protection Ag_3PO_4 from photocorrosion. However, this mechanism is usually neglected in the theoretical analysis. Inspired by that, a strategy of Ag_3PO_4-based Z-Scheme photocatalytic system for improving anti-photocorrosion performance has proposed by our group. we firstly present the hole protective anti-photocorrosion mechanism in this system and reveal the function of the micro-environment during photocatalytic reaction.

In this study, we fabricate a well-designed Z-Scheme photocatalytic system composed of reduced graphene oxide-enwrapped Ag_3PO_4 (Ag_3PO_4@RGO) and La,Cr-codoped $SrTiO_3$ (La,Cr:$SrTiO_3$) successfully. The unique ternary Z-Scheme architectures could effective transport electrons away from Ag_3PO_4 via RGO timely and consumed by holes in La,Cr:$SrTiO_3$, result in enhanced separation efficiency of electron-hole pairs and the formation of rich-hole region on the surfaces of Ag_3PO_4. The rich-hole micro-environment with function as protective layer could protect Ag_3PO_4 from the photo-reduction. Both the carrier separation and the formation of rich-hole micro-environment contribute to the superior photocatalytic and anti-photocorrosion performances in degradation of both RhB and 2,4-DNP under sunlight irradiation. Also, the influences of K^+, Na^+, Cl^-, SO_4^{2-}, NO_3^- and Cr^{6+} have been studied considering that real polluted water contains a variety of inorganic salts. The results show that high-concentration Cl^- and Cr^{6+} ions can significantly decrease photocatalytic activity of this system, and the others do not. This work provides a new application of Z-Scheme photocatalytic system for protection of photosensitive semiconductors from photocorrosion and effective elimination of environmental pollutants under the natural light irradiation. Hence, it can be regard as a new efficient, green and low cost method for wastewater cleaning. Moreover, this strategy also could be applied to other unstable semiconductors and even could extend to outdoor or indoor air cleaning in the future.

2. Experimental

2.1. Chemicals

All chemicals used were analytic grade reagents without further purification; Strontium acetate hemihydrate ($Sr(Ac)_2{\cdot}0.5H_2O$, 98%) were purchased from Alfa Aesar (china) Chemicals Co. Ltd. Titanium tetraisopropanolate ($[(CH_3)_2CHO]_4Ti$) were purchased from shanghai Mackin Biochemical Co. Ltd. All the other reagents were purchased from Sinopharm Chemical Reagent Co. Ltd.

2.2. Preparation of silver phosphate (Ag_3PO_4)

In a typical synthesis [8], Na_2HPO_4 aqueous solution (10 mL, 0.2 M) was slowly added dropwise to the $AgNO_3$ aqueous solution (10 mL, 0.6 M) with magnetically stirring, until the solution turned golden. The precipitates were collected, washed with distilled water several times, and dried in vacuum (70 °C) overnight.

2.3. Preparation of Ag_3PO_4@RGO

Firstly, GO was synthesized according to the improved Hummers method [16]. Secondly, a certain amount of GO was dispersed into deionized water and sonicated for 3 h to give a GO aqueous suspension. Thirdly, 10 mL, 0.6 M $AgNO_3$ aqueous solution was added to the above GO aqueous suspension with vigorous stirring for 12 h. And then Na_2HPO_4 aqueous solution (10 mL, 0.2 M) was added dropwise to the mixture with keeping stirring for 1 h and then irradiated for 15 min under visible light. Finally, The obtained precipitate was washed with distilled water several times, and dried in vacuum (70 °C) overnight. Ag_3PO_4@GO composites were obtained by a similar method except without photocatalytic reduction treatment.

2.4. Preparation of $SrTiO_3$ and La,Cr:$SrTiO_3$

This synthetic method is referred to previous reports [17], and flowchart of the preparation of $SrTiO_3$ and La,Cr:$SrTiO_3$ powders are shown in Fig. S1.

2.5. Preparation of Ag_3PO_4@RGO@La,Cr:$SrTiO_3$

A certain amount of Ag_3PO_4@RGO and La,Cr:$SrTiO_3$ were dispersed into deionized water and sonicated for 30 min, and then a certain amount PVP was added into the Ag_3PO_4@RGO aqueous solution with magnetically stirring for 0.5 h. Finally, La,Cr:$SrTiO_3$ aqueous solution was added dropwise to mentioned above solution and the obtained samples were dried in vacuum (70 °C) overnight.

The procedure for the synthesis of different samples is illustrated in Fig. S2.

2.6. Characterization

The crystal structures and chemical composition characterization of as-prepared samples were determined by X-ray diffraction (XRD) with Cu-Kα radiation (Rigaku, Smartlab), and X-ray photoelectron spectroscopy (XPS) with Al-Kα radiation (Thermo Fisher Scientific, England). The morphologies were determined by field emission scanning electron microscopy (FE-SEM) (Hitachi, S-4800) and transmittance electron microscopy (TEM) (JEOL, JEM-2100F). Raman experiments were performed using a DXR spectrometer with the 532 nm laser line and UV–vis diffuse-reflectance spectra (DRS) were recorded within the 300–800 nm wavelength range using UV–vis spectrophotometer (Cary 300, Varian). The photoluminescence (PL) spectra were measured by using Hitachi F-7000 fluorescence spectrophotometer. Electron spin resonance (ESR) spectra were obtained on a JES FA200 electron paramagnetic resonance spectrometer. Electrochemical measurements were performed in 0.5 M Na_2SO_4 electrolyte solution in a typical three-electrode system that consisted of a working electrode, a platinum wire counter electrode and a saturated calomel reference electrode. The as-prepared photocatalysts thin film on fluorine-doped tin oxide (FTO) was used as the working electrode. The electrochemical response was recorded with a CHI 660C electrochemical analyzer (CHI Inc., USA).

2.7. Degradation under natural outdoor light

Photocatalytic activities of as-prepared samples were evaluated by the degradation experiment using RhB and 2,4-DNP as typical organic pollutants under natural outdoor light irradiation. Typically, 50 mg of as-prepared powder was added into the reaction solution (50 mL, 10 mg/L RhB or 2,4-DNP). The suspension was stirred for 30 min under dark environment to reach an adsorption-desorption equilibrium. And then transferred to the reaction solution out of the window in our laboratory room (Changsha, in China). Irradiance of light recorded by radiometer (FQ-Z). During degradation, 1 mL of suspension was taken out at a given interval time and separated through centrifugation (4000 rpm,

15 min). The concentration of reactant remained in supernatants was analyzed by UV–vis spectrophotometer.

2.8. Degradation under artificial visible light irradiation

The procedure of pollutant degradation is also carried out under a 300 W Xe lamp with a cut off filter (λ > 420 nm) irradiation, which the irradiance is measured to be approximately 750 w/m^2. While the other conditions are the same as those above.

3. Results and discussion

3.1. Characterizations of the as-prepared samples

The microstructure of as-prepared samples was investigated using field-emission scanning electron microscopy (FESEM). Sphere-like Ag_3PO_4 particles (400–500 nm in diameter) could be observed in Fig. 1a. Interestingly, After RGO has been introduced into this system, well-defined Ag_3PO_4 crystals particle were completely wrapped with the gauze-like RGO nanosheets. (Fig. 1b) This can be attributed to the electrostatically-driven self-assembly between Ag^+ and negatively charged GO nanosheets [18], and then GO nanosheets could be reduced into RGO during photocatalytic reduction process. It is worth note that the presence of RGO causes a slight decrease in the size of Ag_3PO_4 particles in the Ag_3PO_4@RGO composites (Fig. 1b). The result implies that RGO play an important role in morphology and size control of Ag_3PO_4 particles, which is beneficial for photocatalysis process.

Fig. 1c shows that the La,Cr:$SrTiO_3$ consists of sphere-like particles aggregates (50–200 nm) of small nanoparticles (40–50 nm). Fig. 1d shows the SEM picture of Ag_3PO_4@RGO@La,Cr:$SrTiO_3$ composite and we can clearly observe that La,Cr:$SrTiO_3$ particles were closely distributed on the surface of RGO nanosheets, which is necessary for effective construction of Z-Scheme photocatalysis system. To further clarify the contact between La,Cr:$SrTiO_3$ and Ag_3PO_4@RGO, TEM characterization technique was applied, as shown in Fig. 1e. The image shows that La,Cr:$SrTiO_3$ and Ag_3PO_4@RGO are well contacted, which facilitates the transfer of charge at the interface. Moreover, the EDS pattern demonstrates that as-prepared samples consist of elemental Ag, P, O, La, Cr, Sr and Ti (Fig. 1f).

Fig. 2a shows the X-ray diffraction (XRD) patterns of as-prepared samples. It can be clearly seen that both the pure $SrTiO_3$ and La,Cr:$SrTiO_3$ samples possess a typical perovskite crystal structure. The positions of diffraction peaks are almost the same for $SrTiO_3$ compared to La,Cr:$SrTiO_3$, which indicates the La and Cr successfully doped into the $SrTiO_3$ crystal structure because La(1.032 Å) and Cr(0.615 Å) substitute the Sr(1.180 Å) and Ti(0.605 Å), respectively [17,19]. In addition, all the diffraction peaks of Ag_3PO_4 could be indexed to the body-centered cubic structure (JCPDS NO.06-0505). No notably characteristic diffraction peaks of RGO, however, are observed in the pattern, which could attribute to the relatively low amount and diffraction intensity of RGO [8]. Raman test was performed to further demonstrate that the presence of RGO and RGO could be obtained by the reduction of GO. The two typical characteristic peaks of GO at 1350 cm^{-1} (D peak) and 1590 cm^{-1} (G peak) could be observed in Fig. 2b. The D/G intensity ratio increase from 1.02 (GO) to 1.17 (RGO), suggesting the transform of GO to RGO [8,20]. Moreover, several peaks appear in the region less than 1300 cm^{-1} are attributed to Ag_3PO_4 [8,21].

All signals of Ag, P, O, C, Sr, and Ti except La and Cr are clearly observed in the full XPS spectrum of the sample (Fig. 3a), which is consistent with the EDS result. To further prove the existence of La and Cr and investigate their chemical states, high-resolution XPS spectra of La 3d (Fig. 3c) and Cr 2p (Fig. 3d) are provided. The two typical peaks at 856.0 and 572.8 eV can be attributed to binding energies of La 3d and Cr 2p, respectively. The results indicate that La and Cr successfully doped into the $SrTiO_3$ crystal structure, which is also in accordance with the XRD result. In addition, Ag $3d_{5/2}$ and Ag $3d_{3/2}$ are located at 367.8 eV and 373.82 eV respectively (Fig. 3b), which are attributed to Ag^+ [22].

The UV–vis absorption spectra of as-prepared samples could be observed in Figs. 4 (a, b) and 5 a . As shown in Fig. 4a, Ag_3PO_4 and Ag_3PO_4@RGO composites both exhibit excellent absorption in the region less than 500 nm specially, there is a distinct enhanced absorbance form about 500 nm to 800 nm for Ag_3PO_4@RGO composite compared with bare Ag_3PO_4. This result implies that RGO nanosheets successfully incorporate into Ag_3PO_4 [18]. Moreover, the absorption band edge of $SrTiO_3$ is about 380 nm while it shifted to 580 nm when doped with La and Cr and the color of $SrTiO_3$ also from white transform to yellow (inset in Fig. 4c). This result convincingly demonstrates that La and Cr successfully doped into the crystal structure of $SrTiO_3$ and the donor levels formed above the valence band of it because of doping of Cr^{3+} impurity [19,23,24]. It's worth noting that the doping of La in $SrTiO_3$ was to inhibit the generation of Cr^{6+}, which could be considered to be unfavorable for photocatalytic reaction [25,26]. Moreover, Ag_3PO_4@RGO@La,Cr:$SrTiO_3$ shows the most intense absorption in the region from 500 nm to 800 nm compared with Ag_3PO_4 and Ag_3PO_4@RGO (Fig. 5a). Surprisedly, the absorption band edge of it shifted to nearly 800 nm, which greatly improves the light utilization of the material. The reason could be ascribed to the band matching and reasonable structure configuration of each component. The Eg values of as-prepared samples were calculated by the Kubelka-Munk method [27] as shown in Fig. 4c. Firstly, the value of n was determined by ln(αhv) vs ln(hv − Eg) plot and the value of Eg was chosen as 2.45 eV. As shown in inset in Fig. 4(a, b), all of the slope of the straightest line is about 1, indicating direct absorption. Secondly, according to the hv axis intercept of the $(\alpha hv)^{1/2}$ vs hv plot, Eg values of the samples were estimated to be 2.32 eV, 3.2 eV and 2.26 eV corresponding to Ag_3PO_4, $SrTiO_3$ and La,Cr:$SrTiO_3$ composite, respectively. Mott-Schottky plot was utilized to characterize the flat band potential [28], which usually is approximate to the conduction band of n-type semiconductors ($CB \approx U_{fb} - 0.2$ V) [29]. As shown in Fig. 4(d–f), the positive slope of the Mott-Schottky plot for all samples indicates n-type nature. The U_{fb} is calculated according to the intercept of the plot with the horizontal axis. The U_{fb} of the samples are 0.2 V, −0.82 V and −0.8 V for Ag_3PO_4, $SrTiO_3$ and La,Cr:$SrTiO_3$ composite, respectively. Thus, the values of CB were determined to 0 V, −1.02 V and −1 V vs SCE, namely, they are 0.24 V, −0.78 V and −0.76 V vs NHE (Normal Hydrogen Electrode). Therefore, the values of VB are 2.56 V, 2.42 V and 1.5 V, respectively. Detailed calculation method was provided in Supplementary Information.

As shown in Fig. 5b, the strong luminous peak was observed at around 535 nm, which arise from the recombination of photogenerated electrons and holes [30,31]. Interestingly, the fluorescence intensity of Ag_3PO_4@RGO and Ag_3PO_4@RGO@La,Cr:$SrTiO_3$ composite, especially for the latter, are greatly reduced compared with that of sole Ag_3PO_4. This result indicates that the low recombination of electron-hole pairs of photocatalyst, which is beneficial for the improvement of photocatalytic performance [32].

3.2. Degradation of RhB dye solution

3.2.1. Under artificial visible light irradiation (λ > 420 nm)

In comparison with sole Ag_3PO_4, Ag_3PO_4@RGO and Ag_3PO_4@RGO@La,Cr:$SrTiO_3$ composites both exhibit superior photocatalytic activities and the optimize mass ratios of as-prepared samples can be observed in Fig. 6(a, b). Fig. 6c shows the reaction kinetic curves for the samples of Ag_3PO_4, Ag_3PO_4@RGO

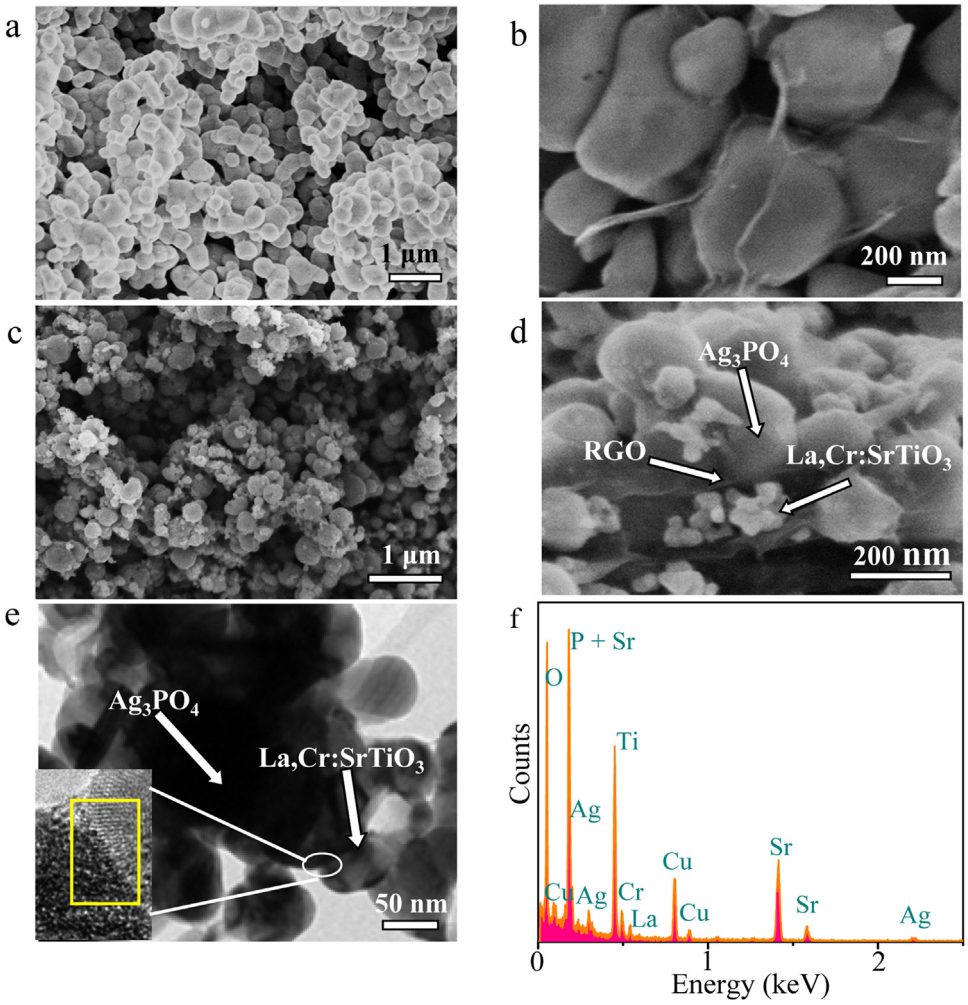

Fig. 1. FESEM images of (a) Ag_3PO_4, (b) Ag_3PO_4@RGO, (c) La,Cr:$SrTiO_3$ composites and (d) Ag_3PO_4@RGO@La,Cr:$SrTiO_3$ composite. e, Typical TEM image of Ag_3PO_4@RGO@La,Cr:$SrTiO_3$ composite. f, energy dispersive spectra (EDS) pattern of Ag_3PO_4@RGO@La,Cr:$SrTiO_3$ composite.

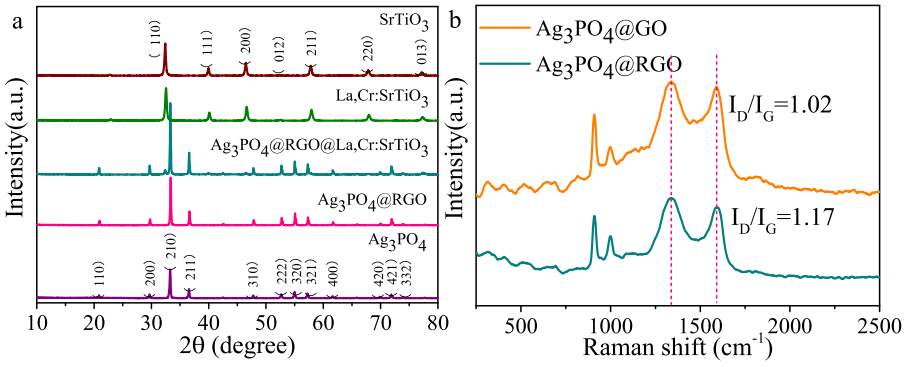

Fig. 2. a, XRD pattern of as-prepared samples. b, Raman spectra of Ag_3PO_4@RGO and Ag_3PO_4@GO.

and Ag_3PO_4@RGO@La,Cr:$SrTiO_3$, of which apparent reaction kinetic constants are calculated to be 0.15, 0.50 and 0.79 (min^{-1}), respectively. Thus, the reaction rate by Ag_3PO_4@RGO@La,Cr:$SrTiO_3$ is faster than that of Ag_3PO_4@RGO and Ag_3PO_4. This results could be attributed to the excellent redox ability, enhancing absorption of visible light and spatial isolation of photogenerated carriers, which achieved in the Z-Scheme photocatalytic system [33,34]. In addition, apparent reaction kinetic constants of as-prepared samples in different content are provided in Table S1. In this system, photogenerated electrons in the conduction band of Ag_3PO_4 could be fast transfer to the donor levels of La,Cr:$SrTiO_3$ via RGO and recombine with photogenerate holes. Meanwhile, the excited electrons in the conduction band of La,Cr:$SrTiO_3$ with excellent reduction ability could react with O_2 to produce the $^{\bullet}O_2^-$ and holes in Ag_3PO_4 with excellent oxidation power could also react with H_2O to produce the $^{\bullet}OH^-$, thereby achieving high efficient degradation of RhB. Notably, $^{\bullet}O_2^-$ could not be produced in Ag_3PO_4 because of the relatively weak reduction potential. Therefore, Ag_3PO_4@RGO@La,Cr:$SrTiO_3$ Z-Scheme photocatalytic system

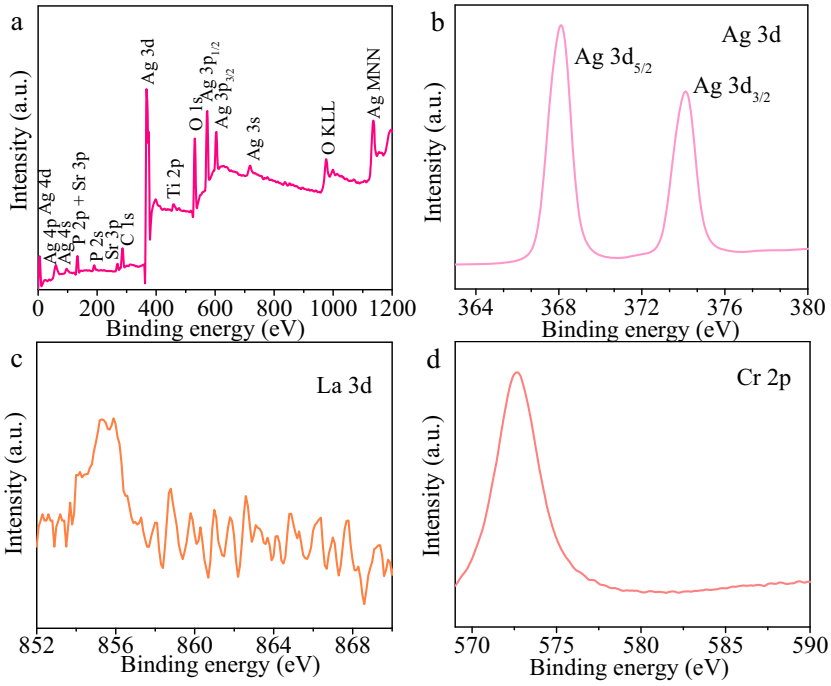

Fig. 3. a, XPS survey spectra. high resolution XPS spectrum of (b) Ag 3d, (c) La 3d and (d) Cd 2p.

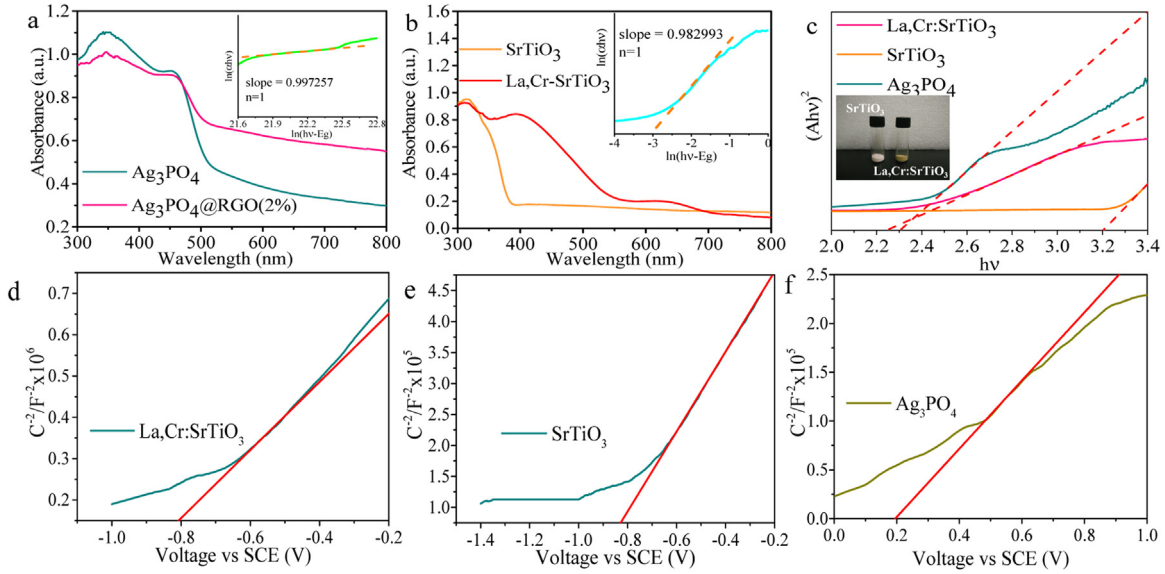

Fig. 4. UV–vis diffuse reflectance spectra of (a) Ag_3PO_4 and Ag_3PO_4@RGO and (b) $SrTiO_3$ and La,Cr:$SrTiO_3$; c, Kubelka-Munk curve of different samples; (d, e and f), the Mott-Schottky plot of different samples.

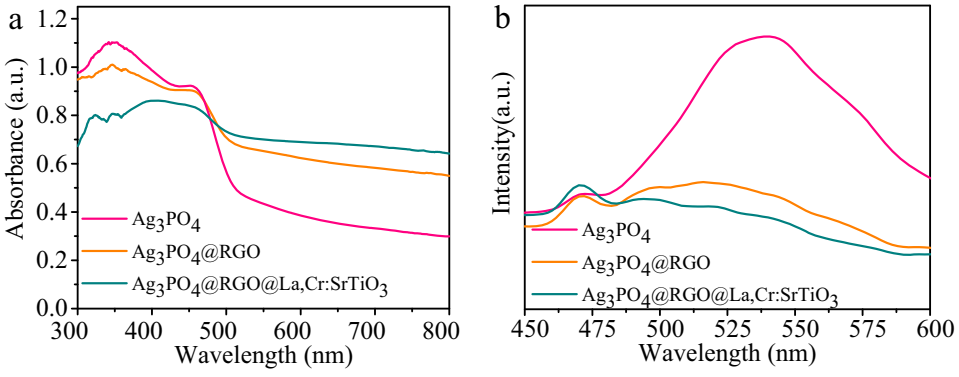

Fig. 5. UV–vis diffuse reflectance spectra (a) and PL spectra (b) of the different samples.

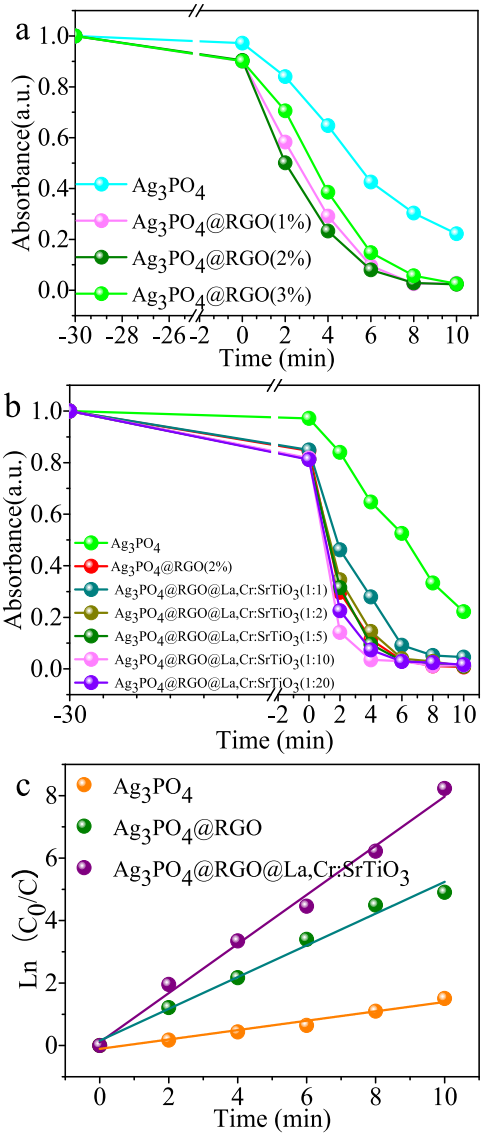

Fig. 6. (a, b), Photodegradation curves of RhB under the artificial visible light irradiation (λ > 420 nm) in the presence of as-prepared samples of different mass ratios; c, reaction kinetic curves of as-prepared samples of optimize mass ratios.

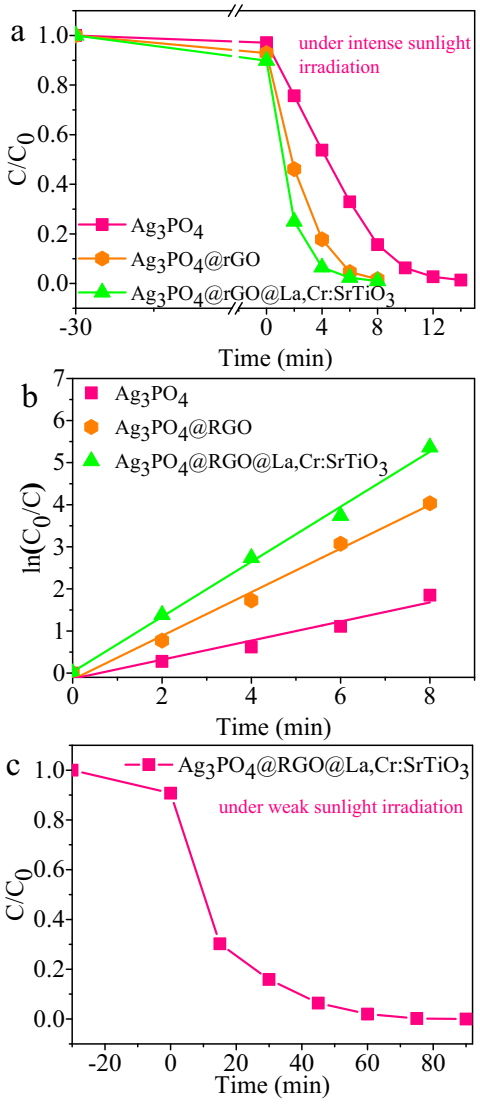

Fig. 7. a, Photodegradation curves of RhB in the presence of as-prepared samples. b, reaction kinetic curves under the natural outdoor intense light irradiation; c, photodegradation curves of RhB under the natural outdoor weak light irradiation in the presence of Ag_3PO_4@RGO@La,Cr:$SrTiO_3$ composite.

exhibits the highest photocatalytic activities for the degradation of RhB compared with Ag_3PO_4 and Ag_3PO_4@RGO.

3.2.2. *Under natural outdoor light irradiation*

We also investigate the degradation performances of RhB solution under natural outdoor light irradiation (Fig. S3). Surprisingly, the results reveal that RhB solution can also be degraded rapidly and completely by as-prepared samples under natural outdoor intense light irradiation, of which irradiance is about 500 w/m^2. Fig. 7 shows the degradation curves and reaction kinetic curves of as-prepared samples. Amazedly, Ag_3PO_4@RGO@La,Cr:$SrTiO_3$ composite shows the highest photocatalytic activities for the degradation of RhB, which only needs about 5 min to completely degrade RhB dye. The apparent kinetic constants for Ag_3PO_4, Ag_3PO_4@RGO and Ag_3PO_4@RGO@La,Cr:$SrTiO_3$ composite are 0.23, 0.52 and 0.65 (min^{-1}) respectively (Fig. 7b). This result prominently demonstrates that as-prepared Ag_3PO_4@RGO@La,Cr:$SrTiO_3$ composite could effectively and adequately utilize natural light to remove organic pollutants because it can take full advantage of two narrow semiconductors. We also further carry out the experiment under the natural weak light irradiation (Location: Hunan University, N28°11′14.26″ E112°57′6.17″; Date: August 14, 2016; Weather: Cloudy.) to study the degradation performances of RhB solution. The irradiance recorded by radiometer are presented in Table S2. Interestingly, RhB also could be degraded completely by Ag_3PO_4@RGO@La,Cr:$SrTiO_3$ composite after only about 70 min under the natural weak light irradiation (Fig. 7c). Thus, it could regard as a green and energy-saving method using silver phosphate-based Z-Scheme photocatalysis systems for environmental cleaning. And the mechanism would be explained in detail in the mechanism section.

3.3. *Degradation of 2,4-DNP solution*

Fig. 8 shows the degradation curves and reaction kinetic curves of as-prepared samples under article artificial visible light irradiation. From Fig. 8a, we can find that the degrading rates of the 2,4-DNP solution by all as-prepared samples are relatively low compared with RhB solution. Especially, La,Cr:$SrTiO_3$ shows little degradation effect toward 2,4-DNP solution, which could be attribute to its relatively weak oxidizing ability lim-

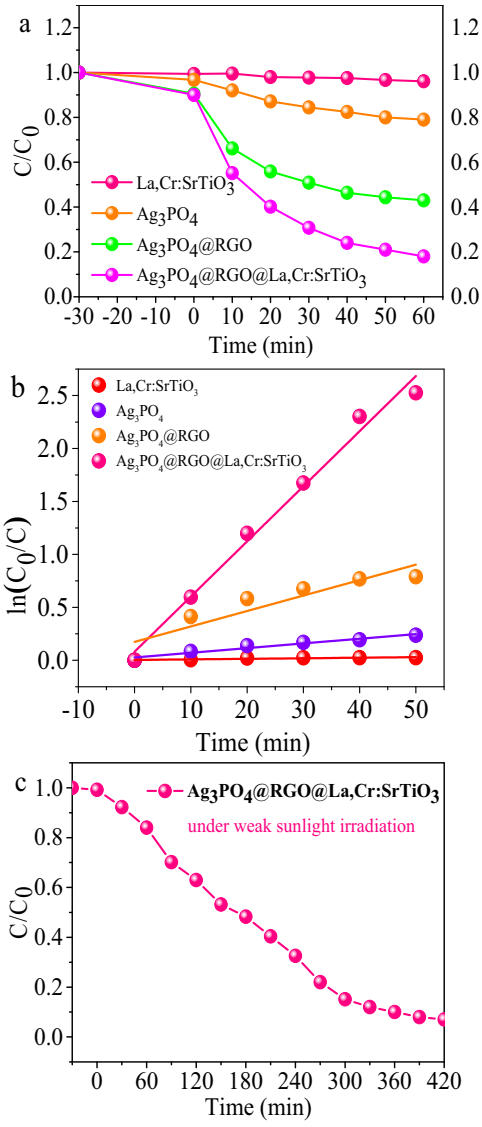

Fig. 8. a, photodegradation curves of 2,4-DNP under artificial visible light irradiation. b, reaction kinetic curves of as-prepared samples. c, photodegradation curves of 2,4-DNP under the nature outdoor weak light irradiation in the presence of Ag_3PO_4@RGO@La,Cr:$SrTiO_3$ composite.

ited by the low position of the valence band (+1.6 V vs. NHE, PH = 7). As shown in Fig. 8b, the apparent kinetic constants for the degradation of 2,4-DNP are 0.052, 0.016, 0.004 and 0.0005 for Ag_3PO_4@RGO@La,Cr:$SrTiO_3$, Ag_3PO_4@RGO, Ag_3PO_4 and La,Cr:$SrTiO_3$, respectively. Namely, the 2,4-DNP photocatalytic reaction rate over Ag_3PO_4@RGO@La,Cr:$SrTiO_3$ composite was the most faster among them. The enhanced performance could be attributed to the synergistic effect of each component in Ag_3PO_4@RGO@La,Cr:$SrTiO_3$ composite and unique ternary Z-Scheme architectures. The detail explanation would be found in the mechanism section of photocatalytic degradation. Fig. 8c also shows the degradation curves of 2,4-DNP over Ag_3PO_4@RGO@La,Cr:$SrTiO_3$ composite under natural outdoor weak light irradiation. The irradiance recorded also could be found in Table S3. From Fig. 8c, we can see that 2,4-DNP solution could be complete degradation under natural outdoor weak light irradiation after about 400 min. The above results have demonstrated that Ag_3PO_4@RGO@La,Cr:$SrTiO_3$ Z-Scheme photocatalysis systems have excellent activity for the degradation of persistent organic pollutant and dye solution even under the natural weak light irradiation due to its ultra-strong redox ability, relatively high carrier separation efficiency, wide absorption range and unique ternary Z-Scheme architectures. Hence, we believe that this Z-Scheme photocatalytic system has the tremendous potential for environmental remediation in practical application.

3.4. Effect of inorganic salts

Generally, some of the inorganic salts which widely exist in the real wastewater will significantly affect the catalysis activities of photocatalysts [35–37]. Thus, the proper amounts of K^+, Cl^-, Cr^{6+}, SO_4^{2-}, NO_3^- and Na^+ ions are added into RhB dye solution respectively to investigate the effects for as-prepared samples. All kinds of ion concentration can be find in Table S4. Fig. 9a shows the degradation curves of RhB solution containing KCl, K_2SO_4, $NaNO_3$ and $K_2Cr_2O_7$ degraded by Ag_3PO_4@RGO@La,Cr:$SrTiO_3$ composite under Xe lamp irradiation ($\lambda > 420$ nm). There is no significant difference found in the degradation curves of the solutions which contain K_2SO_4 and $NaNO_3$, indicating that K^+, SO_4^{2-}, Na^+ and NO_3^- do not affect the degrading performance of Ag_3PO_4@RGO@La,Cr:$SrTiO_3$ composite. Nevertheless, the degrading performance of the composite is sharply decreased when KCl was added into RhB solution, which may be attributed to the strong adsorption of Cl^- on catalyst surface and covered on the surface active site [6]. To further investigate the essential reason of this issue, a series of different concentrations of Cl^- were added into RhB solution during photocatalytic degradation process. It can be obviously observed that as the content of Cl^- increases, the degrading performance of RhB decreases rapidly (Fig. S4a). Note that the color of the as-prepared sample is from yellow transform to gray after reacting with RhB in the presence of KCl (inset in Fig. S4b). As shown in Fig. S4b, the absorbance in 300–800 nm is also become difference before and after the reaction. Therefore, Ag_3PO_4 may be converted to other substances (such as AgCl), leading to the performance decline of samples. In a conclusion, the decline of degrading performance caused by KCl can be mainly attributed to the transformation of Ag_3PO_4. Fig. 9b shows absorption spectra of RhB dye solutions containing Cr^{6+} ions. There is a typical peak of $Cr_2O_7^{2-}$ at about 350 nm and the intensity decreased approximate 76% during the dark adsorption process (30 min). This result clearly uncovers that $Cr_2O_7^{2-}$ also can absorb on the surface of catalysis and also cause a reduction of active site. In summary, the proper concentrations of K^+, Na^+, NO_3^- and SO_4^{2-} do not affect the catalysis activities of Ag_3PO_4@RGO@La,Cr:$SrTiO_3$. However, the existence of certain concentration Cr^{6+} and Cl^-, especially Cl^- ions, would significantly weaken catalysis performance of silver phosphate-based photocatalyst.

3.5. Stability test

The photocorrosion of Ag_3PO_4 has been the key problem to its application because Ag_3PO_4 is slightly soluble in water and the free Ag^+ ion can be easily reduced into Ag by photoelectrons. Hence, the stabilities of Ag_3PO_4 is one of the biggest challenges before putting it into practical applications.

To investigate the stability of Ag_3PO_4 under visible light, RhB is chosen as a model pollutant degraded by as-prepared samples, which is repeated for 5 cycles. As shown in Fig. 10a, there is scarcely any loss in the photocatalytic activity after 5 cycles over Ag_3PO_4@RGO@La,Cr:$SrTiO_3$ composite that can be observed. Nevertheless, a visual decrease of photocatalytic activity can be observed for both bare Ag_3PO_4 and Ag_3PO_4@RGO composite. Especially for Ag_3PO_4, the photocatalytic performance declines by about 75% after 5 cycles, indicating that a large number of Ag_3PO_4 be greatly reduced into Ag^0 by photon-generated electrons. Although it has been reported Ag with Surface Plasmon Resonance (SPR)

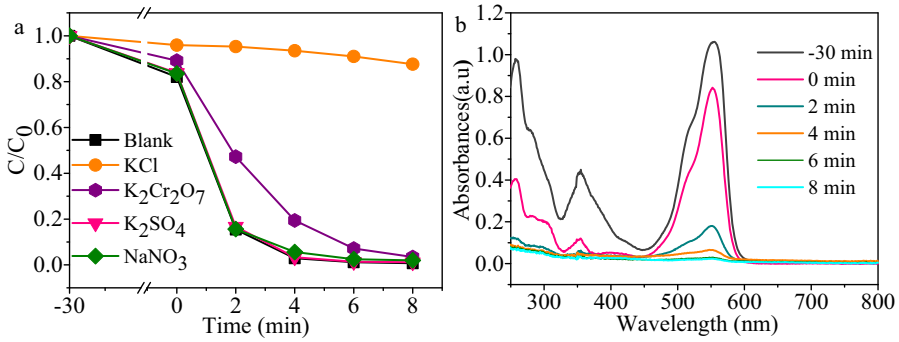

Fig. 9. a, degradation curves of RhB solution containing all kinds of norganic salts. b, absorption spectra of RhB dye solutions containing Cr^{6+} ions in the presents of Ag_3PO_4@RGO@La,Cr:$SrTiO_3$ under artificial visible light irradiation (λ > 420 nm).

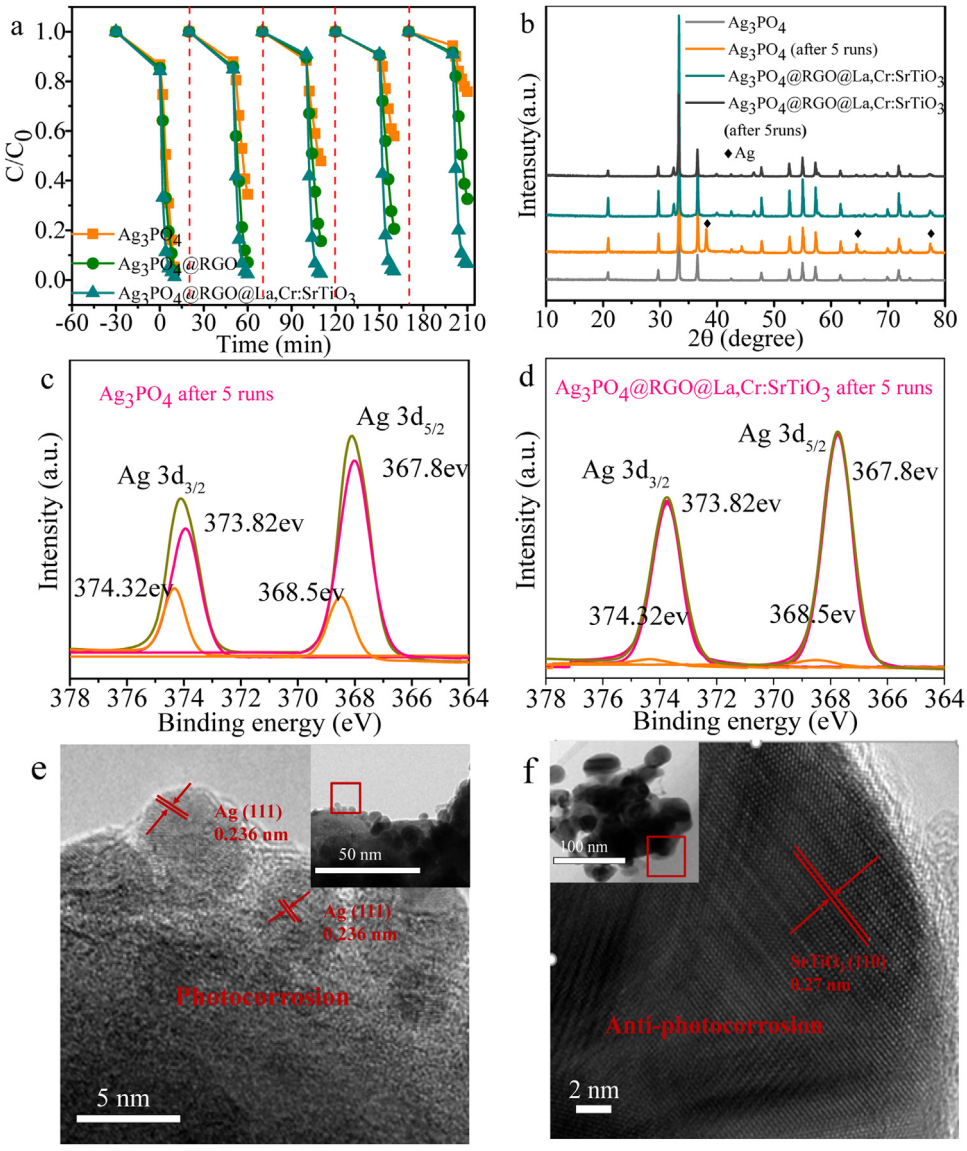

Fig. 10. a, repeated photocatalytic experiments of all kinds of samples. b, XRD patterns of Ag_3PO_4 and Ag_3PO_4@RGO@La,Cr:$SrTiO_3$ after 5 runs. (c, d), XPS spectra of the Ag_3PO_4 and Ag_3PO_4@RGO@La,Cr:$SrTiO_3$ after 5 runs under artificial visible light irradiation (λ > 420 nm). (e, f), TEM images of Ag_3PO_4 and Ag_3PO_4@RGO@La,Cr:$SrTiO_3$ after 5 runs.

effect could enhance and extend the absorption of light [38,39], the decomposing of large amount of Ag_3PO_4 into Ag would decrease the photocatalytic activity of Ag_3PO_4. Namely, the SPR effect caused by Ag could not make up the loss of photocatalytic activity caused by the decreasing in the quantity of Ag_3PO_4. In addition, with the increase of Ag content, there will be a shield layer on the surface of Ag_3PO_4 formed by Ag. The shield layer would block the light absorption of Ag_3PO_4, thereby inhibiting the transfer of carrier between

Ag_3PO_4 and solution. Also it could occupy some active sites of reaction molecules, resulting in the decrease of catalytic activity [40]. XRD patterns of Ag_3PO_4 and Ag_3PO_4@RGO@La,Cr:$SrTiO_3$ after reactions are also shown in Fig. 10b. There are three peaks emerged at 38.1, 64.4 and 77.4 eV for Ag_3PO_4 sample after 5 cycles, which can be classified as characteristic peaks of silver (JCPDS NO.04-0783). Surprisingly, there are no any impurity peak emerged in Ag_3PO_4@RGO@La,Cr:$SrTiO_3$ samples after 5 cycles. Moreover, the XPS spectra of the samples after the reaction were further investigated. Fig. 10c shows the XPS spectra of Ag_3PO_4 after 5 cycles. Two peaks appearing at the 367.8 and 373.82 eV can be attributed to the characteristic peaks of Ag $3d_{5/2}$ and Ag $3d_{3/2}$ respectively, indicating the valence state of Ag is +1. However, the peak located at binding energy of 368.5 and 374,32 eV can be attributed to Ag^0. Comparing Fig. 10c and d, it can clearly observed that the intensities of two peak at 368.5 and 374,32 eV in Ag_3PO_4 is much higher than that of Ag_3PO_4@RGO@La,Cr:$SrTiO_3$. This result shows that a large amount of Ag was formed in Ag_3PO_4 after 5 cycles due to the self-decomposition. In contrast, only a negligible amount of Ag is present in the Ag_3PO_4@RGO@La,Cr:$SrTiO_3$ samples after 5 cycles because of the excellent anti-photocorrosion performance. In addition, Fig. 10e shows the TEM image of Ag_3PO_4 after 5 runs. It can clearly observed that a lot of Ag particles appears on the outer surface of Ag_3PO_4, which confirmed by the high resolution TEM images. In Fig. 10e, it is found that the spacing of adjacent lattice planes is ca. 0.238 nm, which can be ascribed to the interplanar spacing of the (111) planes of cubic Ag, indicating that these nanoparticles are mainly composed of Ag. However, no obvious Ag nanoparticles emerged in Ag_3PO_4@RGO@La,Cr:$SrTiO_3$ samples after 5 cycles. As shown in Fig. 10f, Ag_3PO_4@RGO@La,Cr:$SrTiO_3$ samples maintains a stable structure. Above results powerfully prove that Ag_3PO_4@RGO@La,Cr:$SrTiO_3$ sample is more stable than sole Ag_3PO_4 under the same condition. This could be attributed to the timely and effectively transfer of photoinduced electrons on the surface of Ag_3PO_4 to the surface of La,Cr:$SrTiO_3$ through RGO and then being consumed by the hole on La,Cr:$SrTiO_3$ due to special Z-Scheme electron transfer mechanism. This kind of mechanism would be verified and explained in detail in the section of Z-Scheme electron transfer mechanism.

3.6. Z-Scheme electron transfer mechanism

Generally, to verify the Z-Scheme electron transfer mechanism during photocatalytic degradation, the detection of active oxidant species, superoxide radicals ($^{\bullet}O_2^-$), h^+, and hydroxyl radicals ($^{\bullet}OH$) which are usually considered to be the possible main active oxidant species to degrade organics, could regard as an indirect method [34]. Therefore, RhB was chosen as a model organic to evaluate roles of these active species during photocatalytic degradation process when corresponding scavengers were added to reaction suspensions. Herein, the benzoquinone (BQ), $AgNO_3$, Isopropanol (IPA) and Ethylenediaminetetraacetic acid disodium salt (EDTA) were used as the scavengers for $^{\bullet}O_2^-$, e^-, $^{\bullet}OH$ and h^+, respectively [34,41,42]. The dosages of all sacrificial agent are shown in Table S5. There are little changes of the photodegradation performance when IPA added into reaction suspensions systems, indicating that the $^{\bullet}OH$ play a negligible role in the photocatalytic processes. Similar results are obtained for the Ag_3PO_4@RGO and Ag_3PO_4@RGO@La,Cr:$SrTiO_3$ composites, as shown in Fig. 11(a, b) . However, when BQ and EDTA was added into reaction suspensions systems which used Ag_3PO_4@RGO@La,Cr:$SrTiO_3$ composites as the catalyst, the photodegradation performance was sharply decreased, indicating that h^+ and $^{\bullet}O_2^-$ are main active species for the degradation of RhB (Fig. 11a). However, there is no obvious changes can be observed in the reaction suspensions systems which used Ag_3PO_4@RGO as the catalyst, indicating that $^{\bullet}O_2^-$ could not be produced in this system. Namely, the production of $^{\bullet}O_2^-$ is not caused by RGO (Fig. 11b). The generation of active radicals $^{\bullet}O_2^-$ and $^{\bullet}OH$ is further faithfully confirmed by ESR results. As shown in Fig. 11c, some characteristic peaks of DMPO-$^{\bullet}O_2^-$ were observed in methanol dispersions of Ag_3PO_4@RGO@La,Cr:$SrTiO_3$ composites under visible light irradiation and the signal intensities gradually increased with the increase of time. However, no any signals were detected in dark. Similarly, DMPO-$^{\bullet}OH$ adducts were also detected successfully in aqueous dispersion of this composite, where four characteristic peaks of the DMPO-$^{\bullet}OH$ were observed under visible light irradiation for only 4 min (Fig. 11d). The ESR results suggest that $^{\bullet}O_2^-$ and $^{\bullet}OH$ radicals could be produced by Ag_3PO_4@RGO@La,Cr:$SrTiO_3$ composites under visible light irradiation because of Z-scheme mechanism, which is consistent with radical-trapping photocatalytic experimental results. In order to further confirm the produce of $^{\bullet}O_2^-$ are come form La,Cr:$SrTiO_3$ and $^{\bullet}O_2^-$ could be further transformed into $^{\bullet}OH$. The ESR spectra of La,Cr:$SrTiO_3$ are provided in Fig. S5. As shown in Fig. S5 (a, b), all the signals of $^{\bullet}O_2^-$ and $^{\bullet}OH$ are emerged in this spectra, which powerfully proving the formation of $^{\bullet}O_2^-$ and $^{\bullet}OH$ in La,Cr:$SrTiO_3$ during light irradiation. Hence, probable reactions are:

$$Ag_3PO_4@RGO@La,Cr:SrTiO_3 + h\nu \rightarrow e^- + h^+$$

$$e^- + O_2 \rightarrow {}^{\bullet}O_2^-$$

$$^{\bullet}O_2^- + RhB \rightarrow degradedproducts$$

$$h^+ + RhB \rightarrow degradedproducts$$

This suggests that $^{\bullet}O_2^-$ and h^+ play significant roles in the photocatalytic degradation processes of RhB. If the way of charge carrier transfer between Ag_3PO_4 and La,Cr:$SrTiO_3$ is via heterojunction-type mechanism (Scheme 1a), namely, the photogenarated electrons in the CB of La,Cr:$SrTiO_3$ will migrate to the CB of Ag_3PO_4 fastly through RGO and simultaneously hole on the VB of Ag_3PO_4 will transfer to the donor levels of La,Cr:$SrTiO_3$. As a result, the photogenarated electrons and holes are accumulated in the CB of Ag_3PO_4 and the donor levels of La,Cr:$SrTiO_3$, respectively. This means that photogenarated electrons in the CB of Ag_3PO_4(+0.24 V vs. NHE at pH = 7) cannot reduce O_2 into $^{\bullet}O_2^-$ (−0.28 V vs NHE, PH = 7) [43]. If so, it will not be in agreement with the above experimental results. Therefore, the way of electron transfer in this system was not be the heterojunction-type mechanism. In contrast, if according to Z-Scheme electron-transfer mechanism (Scheme 1b), photogenarated electrons in the CB of Ag_3PO_4 will migrate to the donor levels of La,Cr:$SrTiO_3$ and combine with the photogenareted hole timely. Thus, electrons accumulated in the CB of La,Cr:$SrTiO_3$ (-0.76 V vs NHE at pH = 7) can easily reduce O_2 into $^{\bullet}O_2^-$, which well explains the experimental results that $^{\bullet}O_2^-$ is the main active specie in this reaction system [34]. In addition, to further investigate the role of RGO, Ag_3PO_4@La,Cr:$SrTiO_3$ was prepared to compare with Ag_3PO_4@RGO and Ag_3PO_4@RGO@La,Cr:$SrTiO_3$. The detailed synthetic method is provided in Supplementary Information. Fig. S6a shows the photodegradation curves of RhB in the presence of as-prepared samples under visible light irradiation. It can clearly observed that Ag_3PO_4@La,Cr:$SrTiO_3$ shows the worst degradation activity and adsorption performance compared with Ag_3PO_4@RGO and Ag_3PO_4@RGO@La,Cr:$SrTiO_3$. It also shows the most stronger luminous peak among them (Fig. S6b). In addition, Ag_3PO_4@La,Cr:$SrTiO_3$ shows the worst stability after 5 runs compared with Ag_3PO_4@RGO and Ag_3PO_4@RGO@La,Cr:$SrTiO_3$ (Fig. S6c). Therefore, the role of RGO could be attributed to the following: (i) It enhances the adsorption capacity of materials, improving the degradation of pollutants; (ii) As the electronic media, it can accelerate electron transfer,

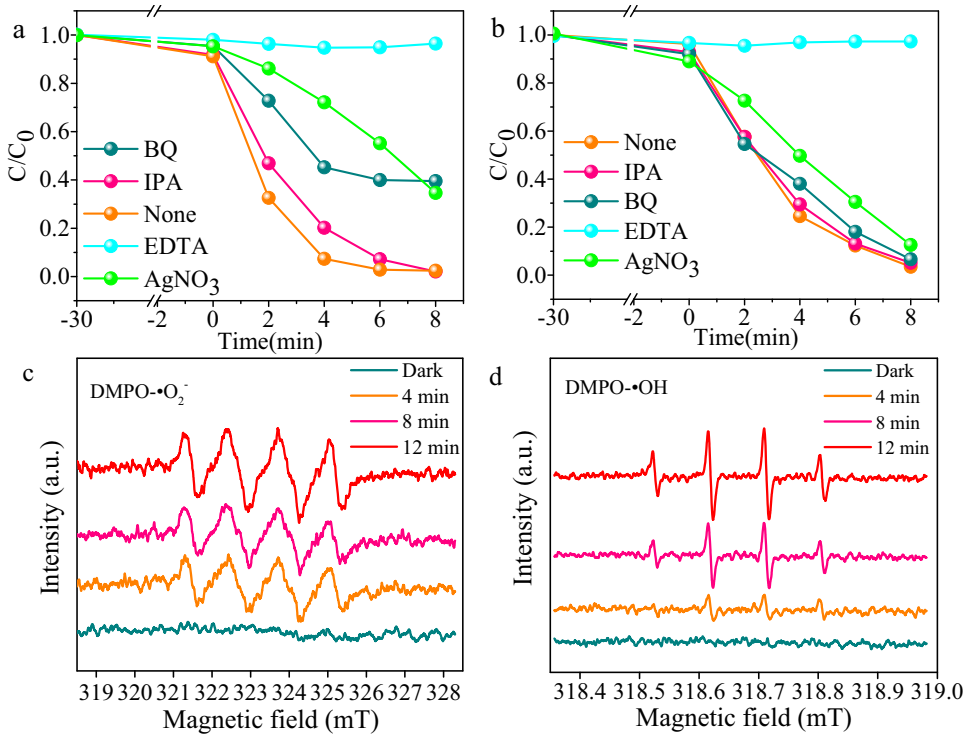

Fig. 11. Degradation curves of RhB with additions of scavengers under visible light over (a) Ag_3PO_4@RGO@La,Cr:$SrTiO_3$ and (b) Ag_3PO_4@RGO. DMPO spin-trapping ESR spectra for (c) DMPO-•OH over Ag_3PO_4@RGO@La,Cr:$SrTiO_3$ in aqueous dispersions and for (d) DMPO-$•O_2^-$ in methanol dispersions.

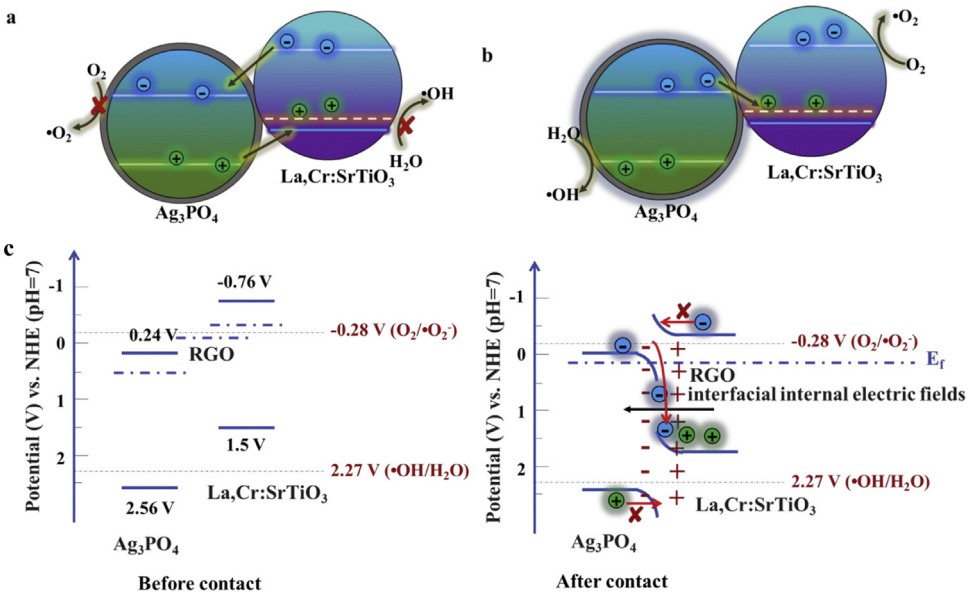

Scheme 1. Diagram of (a) heterojunction-type mechanism, (b) Z-Scheme electron transfer mechanism and (c) detailed Z-Scheme electron transfer mechanism.

which is conducive to the formation of Z-Scheme mechanism, thereby improving the stability of the material. In conclusion, the experimental results demonstrate that the charge carrier transfer mechanism in Ag_3PO_4@RGO@La,Cr:$SrTiO_3$ composites is follow the Z-Scheme electron-transfer mechanism. It also proves that RGO play an important role in adsorption of contaminants and electron transfer of Z-Scheme photocatalysis system. To further understand the electron transfer mechanism, detailed Z-Scheme mechanism based on the theory of interfacial internal electric fields (IEFs) [41] are provided in Scheme 1c. The band positions of samples could be observed in Scheme 1c. After contact of the Ag_3PO_4@RGO and La,Cr:$SrTiO_3$, the electron transfers from the semiconductor with higher fermi level (E_f) to that with lower one. namely, electrons would transfer from La,Cr:$SrTiO_3$ to Ag_3PO_4 and cause shifts of the E_f toward each other and concomitant shifts of the CB and VB, until united E_f is formed (Scheme 1c). In this process, an IEF, with the same direction as the electron transfer, is generated at the Ag_3PO_4@RGO/La,Cr:$SrTiO_3$ interface and makes the bands of photocatalysts bend at the interface. Under visible light irradiation, both the Ag_3PO_4 and the La,Cr:$SrTiO_3$ can be excited. The IEF accelerates the electron transfer from CB of Ag_3PO_4 to VB (donor lever) of La,Cr:$SrTiO_3$, but blocks the electron transfer from CB of

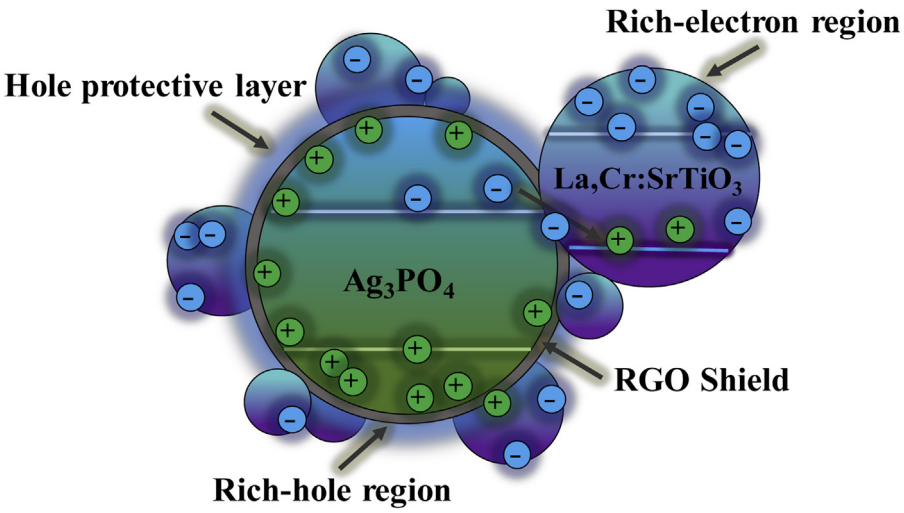

Scheme 2. Photocorrosion-inhibition mechanism.

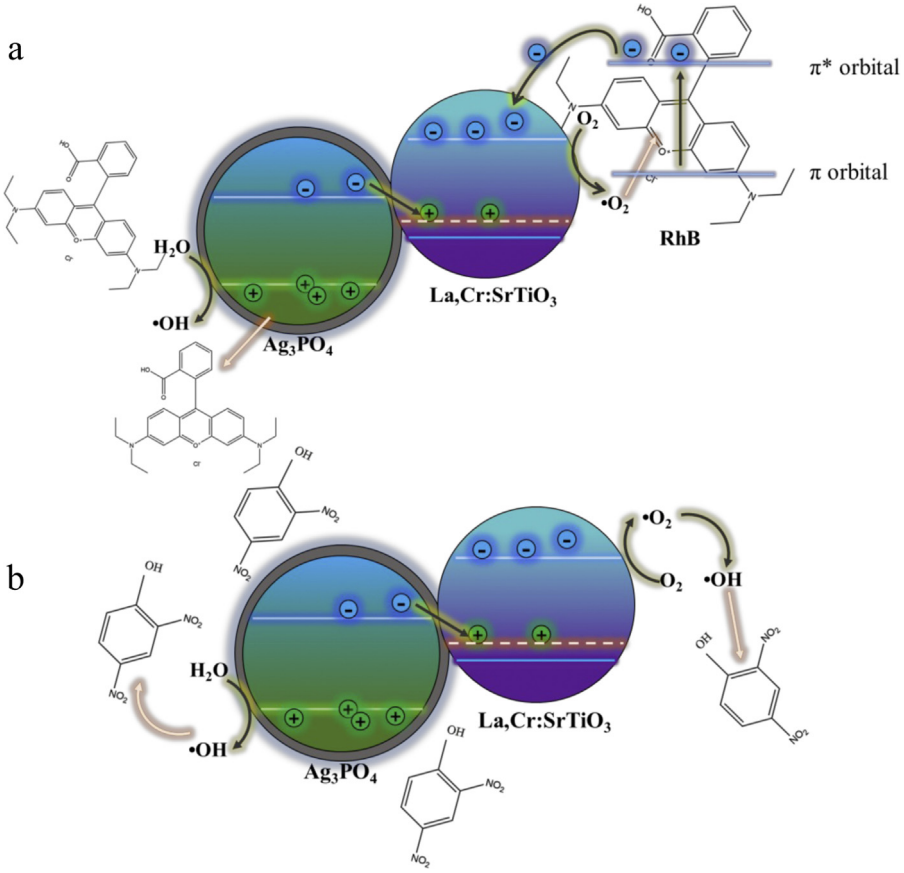

Scheme 3. Diagram of the photocatalytic degradation mechanism of (a) RhB and (b) 2,4-DNP.

$La,Cr:SrTiO_3$ to VB of Ag_3PO_4 due to the role of electric field force. Thereby, electrons and holes in CB of $La,Cr:SrTiO_3$ and VB of Ag_3PO_4 can generate $^{\bullet}O_2^-$ and $^{\bullet}OH$ via reacting with O_2 and H_2O, respectively.

3.7. Anti-photocorrosion mechanism

Photocorrosion problems of Ag_3PO_4 is the deadliest problem that restricting its application. Herein, we proposed a strategy that using silver phosphate-based Z-Scheme photocatalytic system to inhibit the photocorrosion phenomenon which occurs inevitably in Ag_3PO_4. As is shown in Scheme 2, photogenarated electrons in Ag_3PO_4 will migrate to the donor levels of $La,Cr:SrTiO_3$ rapidly via RGO and be consumed timely by recombination with the photogenarated holes, which effectively reduces the chance that contact with Ag^+ ions, thereby inhibiting the photocorrosion to an extent. And more importantly, since photogenarated electrons migrate to the donor levels of $La,Cr:SrTiO_3$ and be consumed by holes, photogenerated holes will aggregate on Ag_3PO_4 and makes Ag_3PO_4 to be an rich-hole region [34], which can suppress the photo-reduction

of Ag_3PO_4. Thus, the aggregation of photogenerated holes on the surface of Ag_3PO_4 will have the similar effect of protective layer, herein, we named "holes-protective layer", which protects Ag_3PO_4 from the attack of photogenerated electrons or electrons existing in environment. In addition, RGO not only play the role of interparticle electron mediator but also function as sheltering layer which can also protect Ag_3PO_4 from photocorrosion. Hence, we firstly synthesize the Ag_3PO_4@RGO@ La,Cr:$SrTiO_3$ Z-Scheme photocatalytic system and demonstrate that this strategy could effectively restrain the photocorrosion of Ag_3PO_4 because of the unique electron transfer paths, reasonable spatial configuration and the synergistic effect of each component. This strategy provides a new thought of dealing with photocorrosion which usually occurs in photosensitive semiconductors and can be applied to other unstable semiconductors.

3.8. Photocatalytic degradation mechanism

The photocatalytic degradation mechanism of RhB was studied in detail in 3.6. It is worth note that RhB dye can also absorb the visible light in the range 460–600 nm, which is attributed to the ground state and the excited state of the dye [44]. Thus, the photocatalytic degradation maybe involves two processes, namely a photocatalytic process and a photosensitized process. On the one hand, RhB could be degraded by the direct interaction with the strong oxidizing hole of Ag_3PO_4. On the other hand, RhB dye could be excited by incident photon flux owing to the intramolecular π-π^* transition. Then, The photoelectrons of the excited state were immediately injected into the CB of La,Cr:$SrTiO_3$, generating O_2^- to mineralize RhB (Scheme 3a). To investigate the photocatalytic degradation mechanism of 2,4-DNP, corresponding scavengers were added to reaction suspensions (The type and quantity of sacrificial agent are the same as the above experiment, see in 3.6). From Fig. S7, it can be observed that photocatalytic performance was sharply decreased when IPA be added into the reaction solution, indicating that $^{\bullet}OH$ is main active specie for the degradation of 2,4-DNP. In contrast, $^{\bullet}O_2^-$ and h^+ play a negligible role in the photocatalytic processes. Therefore, the photocatalytic degradation mechanism of 2,4-DNP is shown as follow:

$$Ag_3PO_4@RGO@La,Cr:SrTiO_3 + h\nu \rightarrow e^- + h^+$$

$$e^- + O_2 \rightarrow {}^{\bullet}O_2^- \rightarrow {}^{\bullet}OH$$

$$h^+ + H_2O \rightarrow {}^{\bullet}OH$$

$$^{\bullet}OH + 2,4\text{-DNP} \rightarrow \text{degradedproducts}$$

And the detailed photocatalytic degradation mechanism is also shown in Scheme 3b.

4. Conclusion

Ag_3PO_4@RGO@La,Cr:$SrTiO_3$ Z-Scheme photocatalytic system was firstly synthesized successfully. It shows excellent photocatalytic activity for both RhB and 2,4-DNP under natural outdoor light irradiation. The high-concentration Cl^- and Cr^{6+} ions can significantly decrease the photocatalytic activity of this Z-Scheme photocatalytic systems. Importantly, this Z-Scheme photocatalytic system shows excellent photochemical stability compared with Ag_3PO_4 due to hole protective mechanism and reasonable spatial configuration in Z-Scheme photocatalytic systems. This strategy provides a new thought of dealing with photocorrosion which usually occurs in photosensitive semiconductors and can also be applied to other unstable semiconductors. Moreover, this strategy could regard as an efficient application method of environmental cleaning for some unstable photocatalysts under natural sunlight irradiation. We believe that this strategy opened a new boulevard for Ag_3PO_4-containing photocatalysts in actual wastewater purification and even could be extended to outdoor or indoor air cleaning in the future.

Acknowledgements

This work was supported by the National Natural Science Foundation of China (51238002, 51378187 and 51478171), Hunan Provincial Natural Science Foundation of China (14JJ1015), and Program for Innovation Research Team in University (IRT1238).

Appendix A. Supplementary data

Supplementary data associated with this article can be found, in the online version, at http://dx.doi.org/10.1016/j.apcatb.2017.02.065.

References

[1] D.J. Martin, G. Liu, S.J. Moniz, Y. Bi, A.M. Beale, J. Ye, J. Tang, Chem. Soc. Rev. 44 (2015) 7808–7828.
[2] Z. Yi, J. Ye, N. Kikugawa, T. Kako, S. Ouyang, H. Stuart-Williams, H. Yang, J. Cao, W. Luo, Z. Li, Y. Liu, R.L. Withers, Nat. Mater. 9 (2010) 559–564.
[3] D.J. Martin, N. Umezawa, X. Chen, J. Ye, J. Tang, Energy Environ. Sci. 6 (2013) 3380.
[4] J. Guo, S. Ouyang, P. Li, Y. Zhang, T. Kako, J. Ye, Appl. Catal. B Environ. 134–135 (2013) 286–292.
[5] F. Teng, Z. Liu, A. Zhang, M. Li, Environ. Sci. Technol. 49 (2015) 9489–9494.
[6] X. Hua, F. Teng, Y. Zhao, J. Xu, C. Xu, Y. Yang, Q. Zhang, S. Paul, Y. Zhang, M. Chen, X. Zhao, Water Res. 81 (2015) 366–374.
[7] Y. Liu, L. Fang, H. Lu, Y. Li, C. Hu, H. Yu, Appl. Catal. B Environ. 115–116 (2012) 245–252.
[8] X. Yang, H. Cui, Y. Li, J. Qin, R. Zhang, H. Tang, ACS Catal. 3 (2013) 363–369.
[9] B. Jiang, Y. Wang, J.-Q. Wang, C. Tian, W. Li, Q. Feng, Q. Pan, H. Fu, ChemCatChem 5 (2013) 1359–1367.
[10] H. Zhang, H. Huang, H. Ming, H. Li, L. Zhang, Y. Liu, Z. Kang, J. Mater. Chem. 22 (2012) 10501.
[11] W. Yao, B. Zhang, C. Huang, C. Ma, X. Song, Q. Xu, J. Mater. Chem. 22 (2012) 4050.
[12] H. Wang, Y. Bai, J. Yang, X. Lang, J. Li, L. Guo, Chemistry 18 (2012) 5524–5529.
[13] A. Iwase, Y.H. Ng, Y. Ishiguro, A. Kudo, R. Amal, J. Am. Chem. Soc. 133 (2011) 11054–11057.
[14] A. Iwase, S. Yoshino, T. Takayama, Y.H. Ng, R. Amal, A. Kudo, J. Am. Chem. Soc. 138 (32) (2016) 10260–10264.
[15] Q. Wang, T. Hisatomi, Q. Jia, H. Tokudome, M. Zhong, C. Wang, Z. Pan, T. Takata, M. Nakabayashi, N. Shibata, Y. Li, I.D. Sharp, A. Kudo, T. Yamada, K. Domen, Nat. Mater. 15 (6) (2016) 611–615.
[16] D.C. Marcano, D.V. Kosynkin, J.M. Berlin, A. Sinitskii, Z. Sun, A. Slesarev, L.B. Alemany, W. Lu, J.M. Tour, ACS Nano 4 (2010) 4806–4814.
[17] S. Ouyang, H. Tong, N. Umezawa, J. Cao, P. Li, Y. Bi, Y. Zhang, J. Ye, J. Am. Chem. Soc. 134 (2012) 1974–1977.
[18] H. Cui, X. Yang, Q. Gao, H. Liu, Y. Li, H. Tang, R. Zhang, J. Qin, X. Yan, Mater. Lett. 93 (2013) 28–31.
[19] S. Tonda, S. Kumar, O. Anjaneyulu, V. Shanker, Phys. Chem. Chem. Phys. 16 (2014) 23819–23828.
[20] Q. Liang, Y. Shi, W. Ma, Z. Li, X. Yang, Phys. Chem. Chem. Phys. 14 (2012) 15657–15665.
[21] Q. Xiang, D. Lang, T. Shen, F. Liu, Appl. Catal. B Environ. 162 (2015) 196–203.
[22] T. Yan, J. Tian, W. Guan, Z. Qiao, W. Li, J. You, B. Huang, Appl. Catal. B Environ. 202 (2017) 84–94.
[23] H. Yu, S. Ouyang, S. Yan, Z. Li, T. Yu, Z. Zou, J. Mater. Chem. 21 (2011) 11347.
[24] M. Muralidharan, V. Anbarasu, A. Elaya Perumal, K. Sivakumar, J. Mater. Sci.: Mater. Electron. 26 (2015) 6352–6365.
[25] U. Sulaeman, S. Yin, T. Sato, Appl. Catal. B Environ. 105 (2011) 206–210.
[26] W. Chen, H. Liu, X. Li, S. Liu, L. Gao, L. Mao, Z. Fan, W. Shangguan, W. Fang, Y. Liu, Appl. Catal. B Environ. 192 (2016) 145–151.
[27] X. Guan, L. Guo, ACS Catal. 4 (2014) 3020–3026.
[28] B. Xu, P. He, H. Liu, P. Wang, G. Zhou, X. Wang, Angew. Chem. Int. Ed. 53 (2014) 2339–2343.
[29] Y. Matsumoto, J. Solid State Chem. 126 (1996) 227–234.
[30] L. Liu, L. Ding, Y. Liu, W. An, S. Lin, Y. Liang, W. Cui, Appl. Catal. B Environ. 201 (2017) 92–104.
[31] S.S. Patil, D.R. Patil, S.K. Apte, M.V. Kulkarni, J.D. Ambekar, C.-J. Park, S.W. Gosavi, S.S. Kolekar, B.B. Kale, Appl. Catal. B Environ. 190 (2016) 75–84.
[32] Y. Bu, Z. Chen, C. Sun, Appl. Catal. B Environ. 179 (2015) 363–371.
[33] K. Maeda, ACS Catal. 3 (2013) 1486–1503.
[34] P. Zhou, J. Yu, M. Jaroniec, Adv. Mater. 26 (2014) 4920–4935.
[35] S. Matsuo, N. Sakaguchi, K. Yamada, T. Matsuo, H. Wakita, Appl. Surf. Sci. 228 (2004) 233–244.

[36] M. Muthukumar, Dyes Pigm. 62 (2004) 221–228.
[37] J. Wiszniowski, D. Robert, J. Surmacz-Gorska, K. Miksch, S. Malato, J.-V. Weber, Appl. Catal. B Environ. 53 (2004) 127–137.
[38] M. Ge, N. Zhu, Y. Zhao, J. Li, L. Liu, Ind. Eng. Chem. Res. 51 (2012) 5167–5173.
[39] Y. Liu, L. Fang, H. Lu, L. Liu, H. Wang, C. Hu, Catal. Commun. 17 (2012) 200–204.
[40] L. Xu, W.-Q. Huang, L.-L. Wang, G.-F. Huang, P. Peng, J. Phys. Chem. C 118 (2014) 12972–12979.
[41] H. Li, T. Hu, R. Zhang, J. Liu, W. Hou, Appl. Catal. B Environ. 188 (2016) 313–323.
[42] S. Ge, L. Zhang, Environ. Sci. Technol. 45 (2011) 3027–3033.
[43] D. Xu, B. Cheng, S. Cao, J. Yu, Appl. Catal. B Environ. 164 (2015) 380–388.
[44] H. Fu, C. Pan, W. Yao, Y. Zhu, J. Phys. Chem. B 109 (2005) 22432–22439.